Effects of Surface Tension on the Richtmyer-Meshkov Instability in Fully Compressible and Inviscid Fluids

Kaito Tang, Wouter Moster, Daniel Fuster, Luc Deike

Effects of Surface Tension on the Richtmyer-Meshkov Instability in Fully Compressible and Inviscid Fluids

Kaitao Tang,[1,2,3] Wouter Mostert,[1,4] Daniel Fuster,[5] and Luc Deike[1,6]

[1]*Department of Mechanical and Aerospace Engineering, Princeton University, Princeton, NJ 08544, USA*
[2]*Center for Combustion Energy, Tsinghua University, Beijing, 100084, China*
[3]*School of Aerospace Engineering, Tsinghua University, Beijing, 100084, China*
[4]*Department of Mechanical and Aerospace Engineering, Missouri University of Science and Technology, Rolla, MO 65401, USA*
[5]*Sorbonne Universités, UPMC Univ Paris 06, CNRS, UMR 7190, Institut Jean Le Rond d'Alembert, F-75005 Paris, France.*
[6]*Princeton Environmental Institute, Princeton University, Princeton, NJ 08544, USA*

(Dated: November 8, 2020)

Novel numerical simulations investigating the Richtmyer-Meshkov instability (RMI) with surface tension are presented. We solve the two-phase compressible Euler equation with surface tension and interface reconstruction by a volume-of-fluid method. We validate and bridge existing theoretical models of surface tension's effects on the RMI in linear, transitional and nonlinear post-shock growth regimes. Under an appropriately constructed dimensional framework, we find good agreement with existing linear incompressible theory in the small-amplitude (linear) oscillatory regime for positive Atwood numbers, and we show that negative Atwood numbers can be accommodated by an appropriate modification to the theory. Next, we show good agreement with nonlinear theory for asymptotic interface growth in the limit of small surface tension. Finally, we heuristically identify a criterion for transition from the linear into the nonlinear oscillation regime. These results highlight the utility of this numerical method for compressible problems featuring surface tension, and pave the way for a broader investigation into mixed compressible/incompressible problems.

I. INTRODUCTION

The Richtmyer-Meshkov instability (RMI) occurs when two regions of fluids with different densities and separated by a perturbed interface undergo an impulsive acceleration, which is often supplied by the passage of a shock wave. The misalignment of the pressure and density gradients incurred by the acceleration results in the baroclinic generation of vorticity deposited on the interface, and hence in the subsequent growth and development of the perturbations.

The RMI is relevant to many applications. It is well-known to inhibit the attainment of fusion in inertial confinement fusion contexts [1]; it can enhance mixing in high-speed airbreathing engines [2]; and may also drive mixing in certain supernovae [3] and magnetic field amplification in supernova remnants travelling through the interstellar medium [4].

If at least one of the fluids is a liquid, or if the interface between the fluids is a membrane [5], surface tension may play a role. This is the case for the familiar example of dropping a bucket filled with water on the ground [6]; the impact on the ground constitutes an impulsive acceleration which promotes the RMI on the water surface. Compressible effects in the gas phase are explicitly involved in the problem of high-speed droplet aerobreakup, which is challenging to investigate both in the laboratory (see Theofanous [7] and references) and numerically [8]. In this connection, the RMI may be relevant to the early-time behaviour of the shocked droplet. In any case, the effect of surface tension on the fine-scale structures at these early times is typically not accounted for by large-scale numerical simulations on grounds of insufficient resolution, even with adaptive mesh refinement (AMR) techniques (see for example Meng and Colonius [8]).

As a fundamental problem, the RMI with surface tension has seen some prior investigation. Mikaelian [5] performed a linear stability analysis of it, finding that the (sufficiently strong) surface tension induces a stable oscillation in the shocked interface whose amplitude and frequency depend on the magnitude of the surface tension. If the surface tension is sufficiently weak, the interface enters a nonlinear growth regime featuring asymmetrically formed narrow "spike" and broad "bubble" structures interpenetrating between the fluids [9, 10]; in this regime, Sohn [11] provided an asymptotic analysis of the velocity of the bubble-structures, and included a brief numerical verification using a phase-field interface model in incompressible fluids [12].

The existing studies reveal only a limited understanding of the RMI with surface tension. First, the stabi-

lizing effect of surface tension on the RMI suggests that it may inhibit transition to the nonlinear regime of bubble and spike development. However, for sufficiently long wavelengths, or sufficiently small surface tensions (corresponding with small values of the Weber number, defined as the ratio between inertial and surface tension forces), the interface perturbations may grow large enough to escape the linear regime before reaching the maximum amplitude of oscillation, so that Mikaelian's analysis [5] no longer applies. This constitutes a *critical Weber number* for the RMI with surface tension, which to our knowledge has not been identified. Second, this critical value will not in general correspond with the vanishingly small surface tension required for Sohn's [11] asymptotic analysis; we expect that there exist cases with intermediately small surface tensions (that is, large Weber numbers) whose perturbation growth patterns are currently not well understood. Finally, none of these studies, which rely on numerical support of theoretical results, consider the effects of compressible flow, which may appear for example in the case of shocked-membrane problems arising in shock tube environments [5], due in part to the lack of compressible-flow solvers that include surface tension effects.

In this study we present fully nonlinear, compressible numerical simulations of the inviscid RMI with surface tension, using Fuster and Popinet's [13] recently developed and implemented numerical technique in the Basilisk package. In addition to the technical significance of this study, its purpose is, firstly, to provide numerical support for the studies of Mikaelian [5] and Sohn [11] in a compressible environment; secondly, to provide insight into the nonlinear development of the problem, considering especially the asymptotic large-time behaviour at small surface tensions (large Weber numbers); and finally, to find the critical Weber number required to suppress the RMI and, in particular, to restrict oscillations of the perturbation to the linear regime.

Our study is structured as follows. In §II we develop a theoretical scaling based on that of Mikaelian [5] to predict the post-shock perturbation growth in the linear phase. In §III we present a formulation of the problem and introduce the numerical method. Afterwards, with the post-shock parameters determined in §IV A, we compare Mikaelian's [5] theory with the scaled numerical results in §IV B, and propose a modified theoretical model based on Vandenboomgaerde et al. [14]. We introduce the theory of Sohn [11] on the perturbation's nonlinear growth, and compare it with the scaled numerical results in §IV C. Then in §IV D we propose a heuristic criterion to delineate the perturbation's develop patterns in its transition to nonlinear growth regime. We eventually conclude the study in §V with some remarks on future work.

II. NON-DIMENSIONAL SCALING MODEL

We first adapt a theoretical result from a linear stability analysis of the incompressible RMI with surface tension, due to Mikaelian [5], into a consistent non-dimensional formulation which can be interpreted in the compressible flow problem featuring a shock wave.

The flow configuration is described in Figure 1, where the fluid to the left is labelled '1', and the fluid to the right labelled '2'. The two inviscid fluids and the sinusoidally perturbed interface are all set to be at rest. The incident shock travels rightwards from the left boundary $x = x_S$ to hit the interface, whose passage will first bring the density and pressure in fluid 1 to intermediate values denoted by subscript 'L'. As is shown in Figure 1(b), after the shock-interface interaction, the interface will be accelerated and acquire a velocity jump Δv; in the meanwhile, part of the shock energy will be transferred into fluid 2 in the form of a transmitted shock, and the rest will reflect back into fluid 1 as a reflected wave, whose passage will bring the density and pressure in fluid 1 to their post-shock values. The perturbed interface will then evolve under the influence of surface tension σ.

The non-dimensional groups governing the problem can be derived with respect to pre- and post-shock state of the interface. We first discuss the pre-shock state, which represents the *a priori* understanding of the system, before next discussing the post-shock state, to which Mikaelian's analysis [5] naturally applies. Afterwards, we will discuss how the post-shock state may be determined from knowledge of the pre-shock state. In the following, minus-sign superscripts denote the pre-shock state, and plus-sign superscripts denote post-shock state.

A. Pre-shock dimensionless parameters

We discuss the state of the problem prior to the shock-interface interface. The density of the pre-shock fluids is given by ρ_i^- $(i = 1, 2)$, and has a dimension of ML^{-3}, where M is mass, L is length and T is time; the unperturbed pressure in each fluid is p_0^- (dimension $ML^{-1}T^{-2}$); and the specific heat ratio of each fluid is Γ_i (dimensionless). The fluids are considered inviscid in this model. The interface which separates the fluids has a monochromatic, sinusoidal perturbation of wavelength λ and amplitude η_0^-, each with dimension L, and

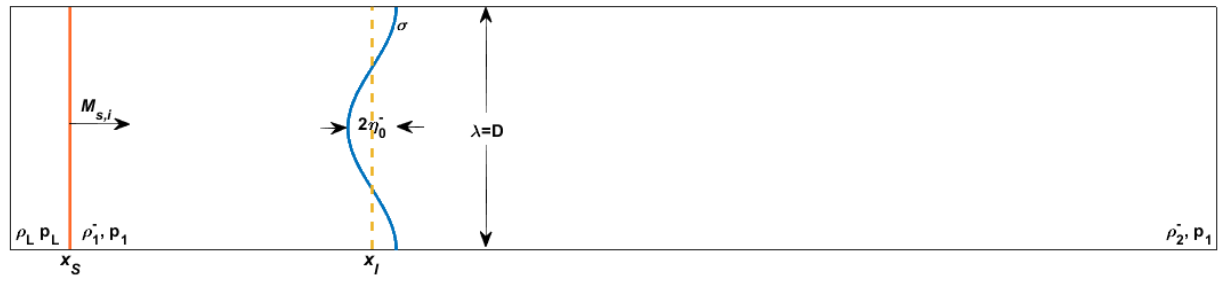

(a)

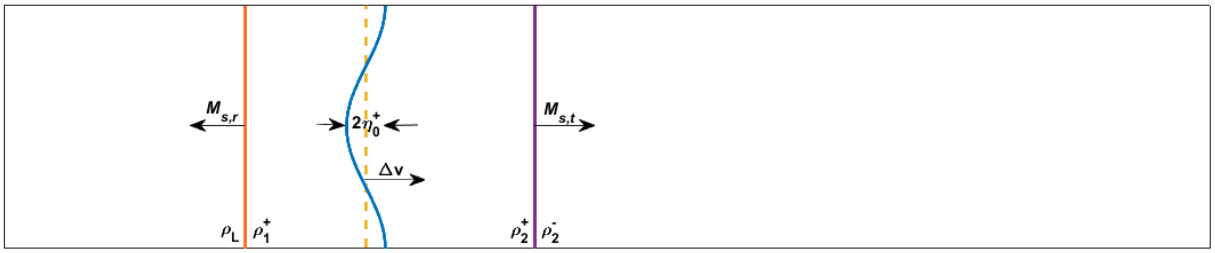

(b)

FIG. 1: Sketches for the pre- (a) and post-shock (b) conditions of the RMI problem with surface tension.

corresponding wavenumber $k = 2\pi/\lambda$ (dimension L^{-1}). The surface tension is given by σ (dimension MT^{-2}). The perturbed interface slightly perturbs the pressure in the two fluid by the action of surface tension; we assume this pressure-perturbation has negligible effect on the subsequent evolution of the system. Finally, the incident shock is planar with a speed $u_{s,I}$ and induces a jump Δu in fluid 1, which is known analytically from the Rankine-Hugoniot shock relations. Applying Buckingham's theorem, we form the following four dimensionless groups apart from Γ_i:

$$s^- \equiv \eta_0^- k = 2\pi \frac{\eta_0^-}{\lambda}, \quad A^- \equiv \frac{\rho_2^- - \rho_1^-}{\rho_2^- + \rho_1^-}, \quad We^- \equiv \frac{\rho_1^- + \rho_2^-}{\sigma k} A^{-2} \Delta u^2, \quad M_{s,I} = \frac{u_{s,I}}{\sqrt{\Gamma_1 p_0 / \rho_1^-}} \tag{1}$$

Here s^- characterizes the slope of the initial perturbed interface; A^- is the Atwood number, which represents the initial density setup; We^- is the Weber number, which measures the strength of surface tension, and $M_{s,I}$ is the Mach number of incident shock.

B. Post-shock dimensionless parameters

We will now discuss the application of Mikaelian's incompressible, impulsive model [5] to the compressible case, and develop the appropriate dimensionless parameters. Mikaelian predicts that, if the perturbation development is in the linear regime (i.e. when the slope s remains small), and the effect of compressibility is negligible after the shock-interface interaction, surface tension as a restoring force will cause the post-shock perturbation amplitude $\eta(t)$ to oscillate sinusoidally,

$$\eta(t) = \eta_0^+ \cos(\omega t) + \frac{\dot{\eta}_0^+}{\omega} \sin(\omega t), \tag{2}$$

where η_0^+ is the post-shock initial perturbation amplitude, and the capillary angular frequency ω is defined in the following form, with post-shock fluid densities ρ_1^+ and ρ_2^+:

$$\omega = \sqrt{\frac{k^3 \sigma}{\rho_1^+ + \rho_2^+}}. \tag{3}$$

$\dot{\eta}_0^+$ is the post-shock initial perturbation growth rate, which Mikaelian [5] gives as,

$$\dot{\eta}_0^+ = \Delta v k A^+ \eta_0^+, \tag{4}$$

where the post-shock Atwood number $A^+ \equiv (\rho_2^+ - \rho_1^+)/(\rho_2^+ + \rho_1^+)$, and Δv is the post-shock velocity jump of the interface. (4) is identical with a version of Richtmyer's [15] prescription for growth rate in the RMI without surface tension.

A set of dimensionless groups to describe the growth characteristics of the RMI can be defined in terms of post-shock variables to be,

$$s^+ = 2\pi \frac{\eta_0^+}{\lambda}, \quad A^+ \equiv \frac{\rho_2^+ - \rho_1^+}{\rho_2^+ + \rho_1^+}, \quad We^+ \equiv \frac{\rho_1^+ + \rho_2^+}{\sigma k} A^{+2} \Delta v^2 \tag{5}$$

These are of the same form as the pre-shock parameters. The time-dependent amplitude $\eta(t) \equiv \eta$ and time t can be included in the non-dimensionalization by,

$$\tilde{\eta} \equiv \frac{\frac{\eta}{\eta_0^+}}{\sqrt{1 + We^+}}, \quad \tilde{t} \equiv \frac{k A^+ \Delta v}{\sqrt{We^+}} t \tag{6}$$

where the tildes indicate nondimensional variables. With these parameters introduced, Mikaelian's model (2) can be summarized in the following normalized form,

$$\tilde{\eta} = \sin\left(\tilde{t} + \arctan\frac{1}{\sqrt{We^+}}\right). \tag{7}$$

Next we discuss how the post-shock parameters may be determined from the pre-shock parameters.

C. Determination of post-shock parameters

It has been concluded in Velikovich [16] that in the weak-shock limit (incident shock's Mach number $M_{s,I} \sim 1$), the pre- and post-shock slope, Weber and Atwood number values are close to each other and there is no need to distinguish between them. It is also in the same weak-shock limit that Richtmyer's prescription is reported to give most accurate results (see for example Figure 1 in Velikovich et al. [17].) In general, however, the post-shock parameters may deviate significantly from the pre-shock values.

Moreover, a change in sign of the pre-shock Atwood number A^- may introduce a qualitative change in the shock interaction process [14, 18, 19]. When the shock wave interacts with the interface, it undergoes a refraction process which results in a transmitted shock and a reflected wave, which may be a shock or a rarefaction wave. The reflected wave type depends on A^- and Γ_i. Drake [18] identifies the following critical pre-shock Atwood number A_c^-,

$$A_c^- = \frac{\Gamma_1 - \Gamma_2}{\Gamma_1 + \Gamma_2 + 2}. \tag{8}$$

When $A^- < A_c^-$, a reflected rarefaction is expected to form in fluid 1; otherwise a reflected shock is expected. Within our work, we set the specific heat ratios as $\Gamma_1 = \Gamma_2 \equiv \gamma = 1.4$, hence $A_c^- = 0$, i.e. negative pre-shock Atwood numbers A^- correspond to reflected rarefactions, and positive ones to reflected shocks.

It has been reported that separate small-amplitude analyses are required for cases with reflected shocks and rarefactions when surface tension is absent [14, 20]. Nevertheless, Mikaelian's model [5] does not distinguish between the two situations and the post-shock parameters (see §II B for definition) are assumed known.

Finally, the post-shock and pre-shock amplitudes η_0^+, η_0^- are discussed by Vandenboomgaerde et al. [14] and Mikaelian [21] and can be related by the compression ratio r, which is derived from the formulations of Richtmyer [15]:

$$r \equiv \frac{\eta_0^+}{\eta_0^-} = 1 - \frac{\Delta v}{u_{s,I}}, \tag{9}$$

where $u_{s,I}$ is the speed of the incident shock, which can be calculated using the pre-shock parameters.

III. FORMULATION AND METHODOLOGY

A. Governing equations

We solve the two-phase compressible Euler equations with surface tension, which are written,

$$\frac{\partial f}{\partial t} + \boldsymbol{u} \cdot \nabla f = 0 \tag{10}$$

$$\frac{\partial \rho_i}{\partial t} + \nabla \cdot (\rho_i \boldsymbol{u_i}) = 0 \tag{11}$$

$$\frac{\partial \rho_i \boldsymbol{u_i}}{\partial t} + \nabla \cdot (\rho_i \boldsymbol{u_i} \boldsymbol{u_i}) = -\nabla p_i \tag{12}$$

$$\frac{\partial}{\partial t}\left(\rho_i e_i + \frac{1}{2}\rho_i \boldsymbol{u_i}^2\right) + \nabla \cdot \left[\boldsymbol{u_i}\left(\rho_i e_i + \frac{1}{2}\rho_i \boldsymbol{u_i}^2\right)\right] = -\nabla \cdot (\boldsymbol{u_i} p_i)\,. \tag{13}$$

The advective equation (10) is applied to determine the interface position, featuring a Heaviside function f, which jumps from 1 (in fluid 1) to 0 (in fluid 2) at the interface. Equations (11) and (12) are respectively the continuity and momentum equation for each fluid (i=1, 2), where p_i is the fluid pressure. The influence of surface tension σ is incorporated into the pressure gradient term by applying the Young-Laplace equation $p_1 - p_2 = \sigma\kappa$ to the grid cells containing the interface, where κ is the local interface mean curvature.

The energy equation (13) is included owing to the presence of compressibility, where e_i denotes the internal energy of each fluid. Equations of state are still required to close the equation system. While both incompressible and compressible fluids can be modeled simultaneously by Mie-Grüneisen equation of state in the numerical solver, for this study we restrict our attention to entirely compressible flow by applying the ideal gas law as a special case:

$$\rho_i e_i = \frac{p_i}{\Gamma_i - 1} \tag{14}$$

B. Numerical method

The simulations in this work are conducted within the open-source solver Basilisk using the all-Mach scheme proposed by Fuster and Popinet [13] for multiphase flows, which is capable of handling mixed compressible-incompressible fluids. This is a second-order accurate finite volume numerical scheme with hyperbolic upwinding suitable for shock capturing. Within the scheme, a Volume of Fluid (VOF) method is used to model the fluid interface, which guarantees a sharp representation of the interface and reduces the parasitic currents induced by surface tension.

The problem is initialized within a rectangular simulation domain of size $nD \times D$, where D is the width of the domain and $n = 5, 7$ or 11, depending on the particular case. The shock is initialized at the left boundary, so that the domain is defined by $\Omega = [x_S, nD + x_S] \times [-D, 0]$. The initial fluid configuration is divided into two fluid regions (Fluid 1 and 2 on the left and right respectively) by an initial regularized Heaviside function f_0. The boundary conditions on the top and bottom of the domain are periodic. We use a zero-gradient boundary condition at the right boundary, while at the left side Dirichlet conditions are applied according to the post-shock conditions for a incident shock of Mach number M_s; these are discussed further below.

The discretized grid size is defined as $\Delta x = D/2^L$, where L is the resolution level. Most of our simulations are conducted on $L = 9$, while for convergence studies we also run certain cases on levels $L = 8$ and $L = 10$ for comparison. The discretized timestep is characterized and controlled by a non-dimensional constant $CFL_{ac} = c_m \Delta t/\Delta x$, where c_m is the expected maximum local speed of sound. For all simulations conducted in this work, we set $CFL_{ac} = 0.5$.

The output files produced by the simulation are collected and processed to reconstruct the interface profile, which allows for analysis of the non-dimensional perturbation amplitude $\tilde{\eta}$ and time $\tilde{t}$ at each time-step.

1. Numerical initialization of the interface and incident shock

The interface between Fluids 1 and 2 is perturbed with a single-mode cosine function, which takes the form of $x(y) = x_I + \eta_0^- \cos ky$. The average position of the interface x_I is set to 0, and the wave number of the single-mode perturbation is set to $k = \frac{2\pi}{D}$, so that the domain spans a single wavelength. For the initial perturbation amplitude η_0^-, we set it sufficiently small to satisfy the linear regime prerequisite $s^- = k\eta_0^- \ll 1$; we choose $\eta_0^- = 0.01$, 0.015 or 0.02, thus allocating approximately 5-10 grids across the initial perturbation profile at resolution level $L = 9$. This is sufficient to capture the growth characteristics of the RMI independent of the numerical resolution, as shown in §A.

As is mentioned in §III A, the interface is tracked by a Heaviside function f that jumps from 1 to 0 at its location. In numerical simulations, we apply a hyperbolic-tangent regularization in the initial interface's neighborhood to smooth the local representation of f in a Cartesian mesh [22], which takes the form of $f_0 = \frac{1}{2}\left(1 - \tanh\left[\frac{N}{8}\left(x - \eta_0^- \cos ky\right)\right]\right)$. Here $N = n(2^L)$ is the number of cells in the long dimension of the rectangular simulation domain. This makes the width of f_0's transition zone approximately the same for different resolution levels.

The incident shock is initialized at the left boundary of the simulation domain $x = x_S$ by assigning the values of ρ_L, q_L, E_L to the conservative variables via the aforementioned Dirichlet boundary conditions. We set the left boundary x_S immediately next to the initial interface at $x_I = 0$, so that the surface-tension-induced self-oscillation behavior does not have sufficient time to influence the interface's pre-shock perturbation amplitude before its interaction with the incident shock.

2. Parameter space

We present the pre-shock non-dimensional parameter space to be investigated in this work. Namely, we conduct the simulations with pre-shock perturbation amplitude values going from low (0.01), medium (0.015) to high (0.02), corresponding to s^- values of 0.02π, 0.03π and 0.04π. We set $M_{s,I} = 2$ (strong-shock) in most situations, where compressibility's influence is already nontrivial but has not yet caused significant deviations from the impulsive model (see Figure 8 in [23]); while also setting $M_{s,I} = 1.2$ (weak-shock) in certain cases to allow for discussions on its influence. Pre-shock Atwood numbers are $A^- = 9/11$ and $-9/11$, where the former is achieved by setting $\rho_1^- = 0.1$, $\rho_2^- = 1$, and the latter by setting $\rho_1^- = 1$, $\rho_2^- = 0.1$. The magnitude of pre-shock Weber numbers We^- we investigate ranges from 10^1 to 10^3, which covers all three of the linear, transitional and nonlinear post-shock growth-rate regime.

IV. RESULTS

A. Post-shock parameters

As mentioned in §II, the post-shock state variables ρ_1^+, ρ_2^+, A^+, Δv and compression ratio r are required to calculate the post-shock dimensionless parameters, and are determined in the present study from numerical diagnostics. While these parameters can be predicted theoretically via (B1),(B2) [21], the theory does not account for surface tension. This topic is discussed further in the appendix, §B.

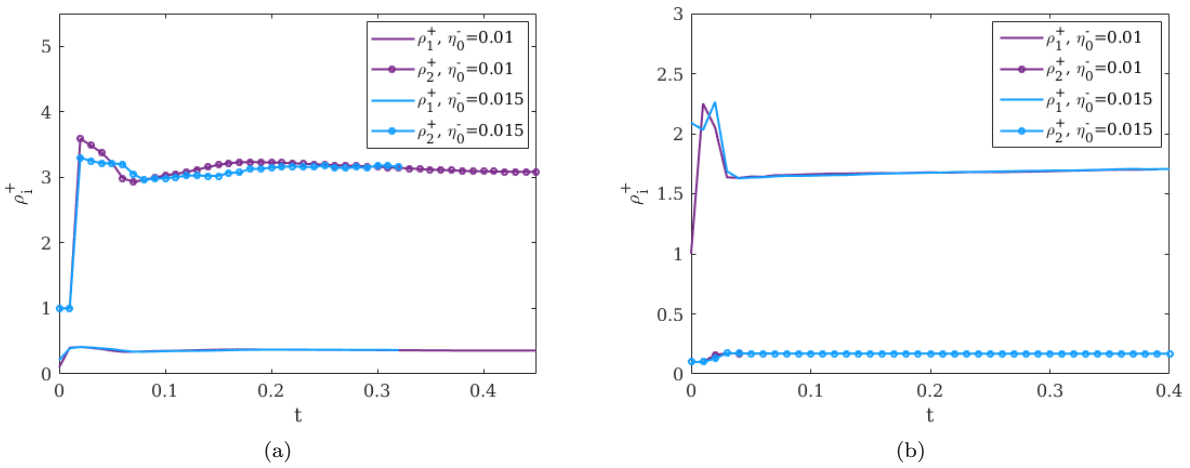

FIG. 2: The development of post-shock density values ρ_i^+ in cases with pre-shock Atwood number $A^- = 9/11$ (a) and $A^- = -9/11$ (b) measured from numerical diagnostics. The post-shock densities of the two fluids are observed to eventually settle down at steady-state values, which are chosen as the post-shock values determined by numerical diagnostics.

In the diagnostics, the post-shock state variables are extracted close to the interface, and averaged over y to remove variations due to the interface perturbation. Figure 2 shows the diagnostic outputs for sample cases with $A^- = \pm 9/11$, $We^- = 159, 239$, and $\eta_0^- = 0.01, 0.015$. All measured variables behave similarly in the diagnostics: there is a short transient period at early times associated with shock-interface interaction, before the measured variables stabilize as the transmitted and reflected wavefronts move away from the post-shock interface. The steady-state values are not affected by the value of η_0^-, as expected, and are taken as the post-shock state. As discussed in the appendix B, these numerical diagnostics are more reliable for the present study than the theory in [21]. Note that, apart from providing information about the post-shock flow fields, the existence of steady-state density values also consolidates the assumption [5] that compressibility's influences are limited to the shock-interface interaction period, and the post-shock flow fields near the interface can be treated as nearly incompressible, which is also confirmed in other numerical results [6, 24].

B. Linear regime

We now test the normalized model of Mikaelian [5] in the form of (7), which predicts that the scaled $\tilde{\eta} - \tilde{t}$ curves with different Atwood, Weber and Mach numbers will show good collapsing (provided that the post-shock Weber number We^+ is sufficiently large for the phase shift term $\Delta\varphi = \arctan 1/\sqrt{We^+}$ to vanish), with peaks at $\tilde{\eta} = 1$.

The results are presented in Figure 3, where they are organised into three major categories: strong shock ($M_{s,I} = 2$) with negative Atwood number ($A^- = -9/11$) in the first row, strong shock with positive Atwood number ($A^- = 9/11$) in the second and weak shock ($M_{s,I} = 1.2$) with positive Atwood number in the third row. For each Atwood/Mach number category, a sweeping of Weber number We^- is conducted, with the dimensional $\eta - t$ curves plotted in the left column (Figures 3(a), 3(c), 3(e)) and the scaled curves according to Equation (6) shown in the right (Figures 3(b), 3(d), 3(f)). To facilitate comparison of simulation results with Mikaelian's model [5], we also plot the $\tilde{\eta} - \tilde{t}$ curves predicted by (7) in dashed lines, for which the phase shift term $\arctan 1/\sqrt{We^+}$ is neglected. In the legend regions, the Weber number values outside the parentheses indicate pre-shock value We^-, while their counterparts within the parentheses indicate post-shock value We^+.

In the following parts, we will first discuss the influence of Atwood number A^- on post-shock perturbation growth in IV B 1 by comparing the first and second row in Figure 3, and then the influence of incident shock's Mach number $M_{s,I}$ in IV B 2 by comparing the second and third row of the same figure.

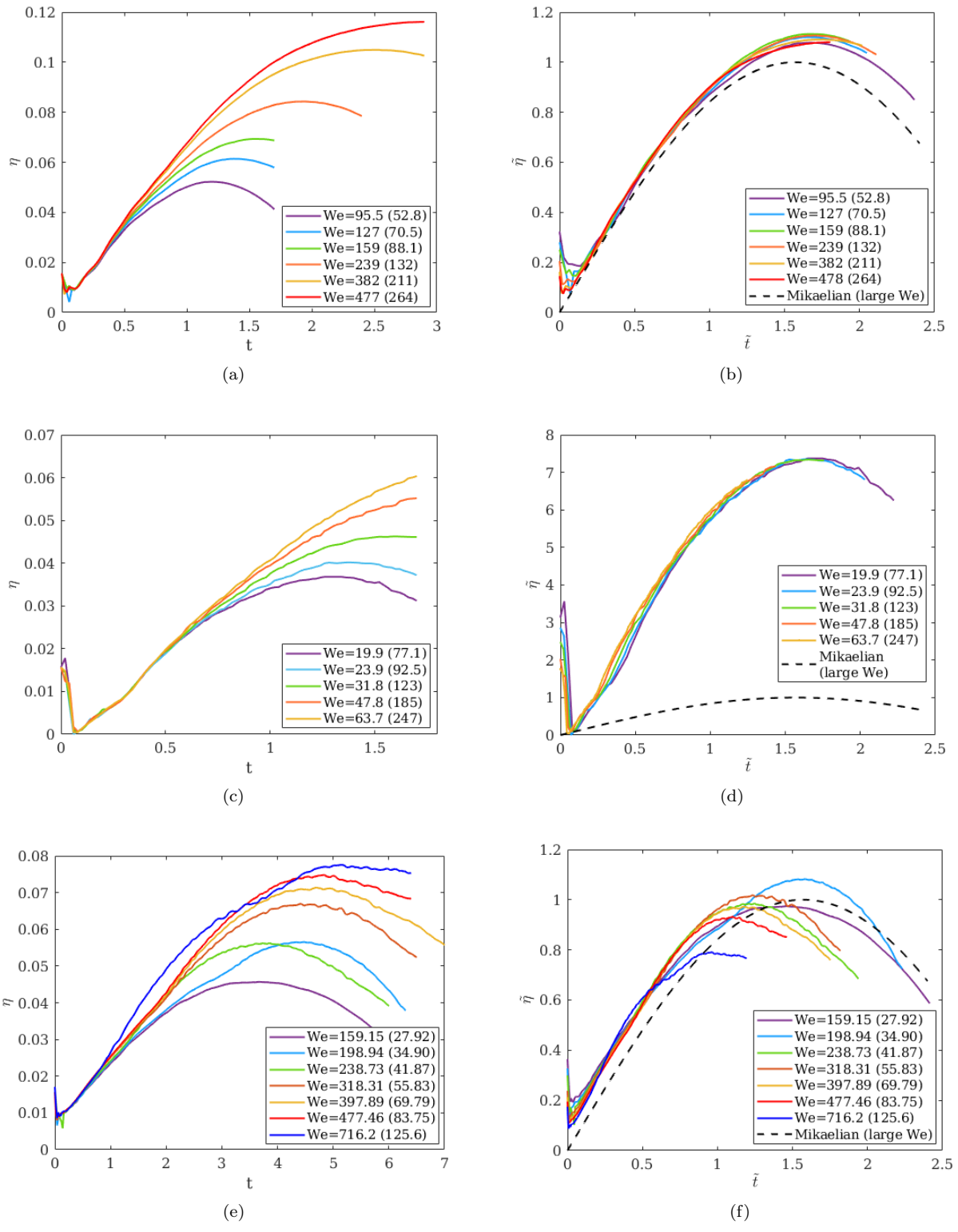

FIG. 3: Numerical results compared with Mikaelian's theory [5]. Upper row: strong shock ($M_{s,I} = 2$) with negative Atwood number ($A^- = -9/11$); middle row: strong shock ($M_{s,I} = 2$) with positive Atwood number ($A^- = 9/11$); lower row: weak shock ($M_{s,I} = 1.2$) with positive Atwood number ($A^- = 9/11$). Left column: raw outputs; right column: normalized results. Good collapsing patterns are observed for strong-shock cases ($M_{s,I} = 2$), among which those with positive Atwood number $A^- = 9/11$ show a good qualitative agreement with Mikaelian's theory [5]; whereas the weak-shock cases display poor collapsing under the normalization.

1. Effect of initial fluid density configuration

As is shown in Figures 3(a) and 3(c), the post-shock perturbation amplitude η will first increase with diminishing growth rate. At small post-shock Weber number We^+, η will reach a peak and then decrease, whereas for large We^+ values the peak will not be reached in the limited simulation domain. These findings agrees with the numerical results of [25].

When the $\tilde{\eta}-\tilde{t}$ curves are normalized, they overlap very well for both positive and negative Atwood number cases with $M_{s,i} = 2$. However, discrepancy exists between the two Atwood number classes: the positive Atwood number cases have their first normalized peaks around $\tilde{\eta} = 1.1$ (Figure 3(b)), while those of the negative Atwood number cases are much higher, being around $\tilde{\eta} = 7.3$ (Figure 3(d)). Consequently, the positive Atwood number cases conform to Mikaelian's model (7) more closely, whereas the negative Atwood number cases show a nontrivial deviation from the same model.

This negative-Atwood discrepancy is rooted in the incompressible nature of Mikaelian's model [5], and might be traced further back to the situations where surface tension σ is absent. As the post-shock Weber number We^+ asymptotically approaches infinity, Mikaelian's model [5] will reduce to Richtmyer's impulsive prescription [15] in the form of Equation (4). Vandenboomgaerde et al. [14] and Velikovich [16] observe that this prescription usually gives good results for positive Atwood number cases, but fails for negative Atwood number cases where $\dot{\eta}$ is not proportional to A^+ [21] and other alternatives are available (e.g. [14, 19, 26]).

We will now seek to develop a correction to the linear theory of [5] that can effectively reduce the discrepancy caused by opposite signs of Atwood numbers. An alternative to Equation (4) is given in [14] as:

$$\eta = \eta_0^+ + k\Delta v \left[\frac{1}{2}\left(A^+\eta_0^+ + A^-\eta_0^-\right) - \frac{1}{6}\left(A^+ - A^-\right)\left(\eta_0^+ - \eta_0^-\right)\right] t \tag{15}$$

In this prescription, the post-shock perturbation growth rate now depends on both pre- and post-shock states, which is different from Mikaelian's model [5], as the latter is only related to the post-shock state. We then seek to compare the performance of Vandenboomgaerde's prescription [14] with Richtmyer's [15] in the zero-surface-tension cases with different Atwood number setups.

As is shown in Figures 4(a) and 4(b), the slope of Vandenboomgaerde's prescription (15) matches better with simulation data in both positive and negative Atwood number cases despite an overestimation for the latter, while Richtmyer's prescription (4) [15] shows a slight underestimation for positive Atwood number and significantly deviates from simulations with negative Atwood number. The underestimation of Richtmyer's prescription [15] corresponds back to the deviation patterns of our simulation data from the scaling model in the previous part, where the $A^- = 9/11$ cases slightly overshoots the theoretical maximum $\tilde{\eta}_{max} = 1$ under the scaling, and those with $A^- = -9/11$ significantly overestimates the same maximum.

Consequently, in order to modify Mikaelian's model [5] for a better performance, we tentatively replace the Richtmyer's prescription embodied in (2) with Vandenboomgaerde's [14]. To this end, we introduce the modified Atwood number $\tilde{A}$ based on Vandenboomgaerde's work [14], which may be viewed as an average of pre- and post-shock Atwood numbers A^- and A^+ involving compression ratio r:

$$\tilde{A} \equiv \frac{1}{2}\left(A^+ + \frac{A^-}{r}\right) - \frac{1}{6}\left(A^+ - A^-\right)\left(1 - \frac{1}{r}\right) \tag{16}$$

With this modified Atwood number defined, the post-shock dimensionless parameters and normalized perturbation-growth model (7) proposed in §II B can be formally retained by replacing all A^+ with $\tilde{A}$.

When the modified model is compared with simulation results, as is shown in Figures 4(c) and 4(d), within each Atwood number category the normalized curves still shows good collapsing, and good agreement is found between the results of the two Atwood numbers with opposite signs, as the first peaks of all normalized curves are now around $(\tilde{t}, \tilde{\eta}) = (1.65, 0.8)$. This maximum $\tilde{\eta}$ value of 0.8 is less than the ideal 1 expected by the modified model, which is likely caused by Vandenboomgaerde's prescription's [14] aforementioned overestimation of $\dot{\eta}_0^+$ in zero-surface-tension cases; but it is still a considerable improvement compared with the original model of Mikaelian [5], especially for negative Atwood number cases since their discrepancy in peak values with positive Atwood ones is now greatly reduced.

If the impulsive base of Mikaelian [5] (2) is to be retained, more accurate models for perturbation growth under the influence of surface tension can be derived by swapping Vandenboomgaerde et al.'s prescription (Equation (16)) for more precise ones, whose proposal is a fundamental problem for RMI studies and require detailed investigation of the shock-interface interaction period, which is out of the scope of this work.

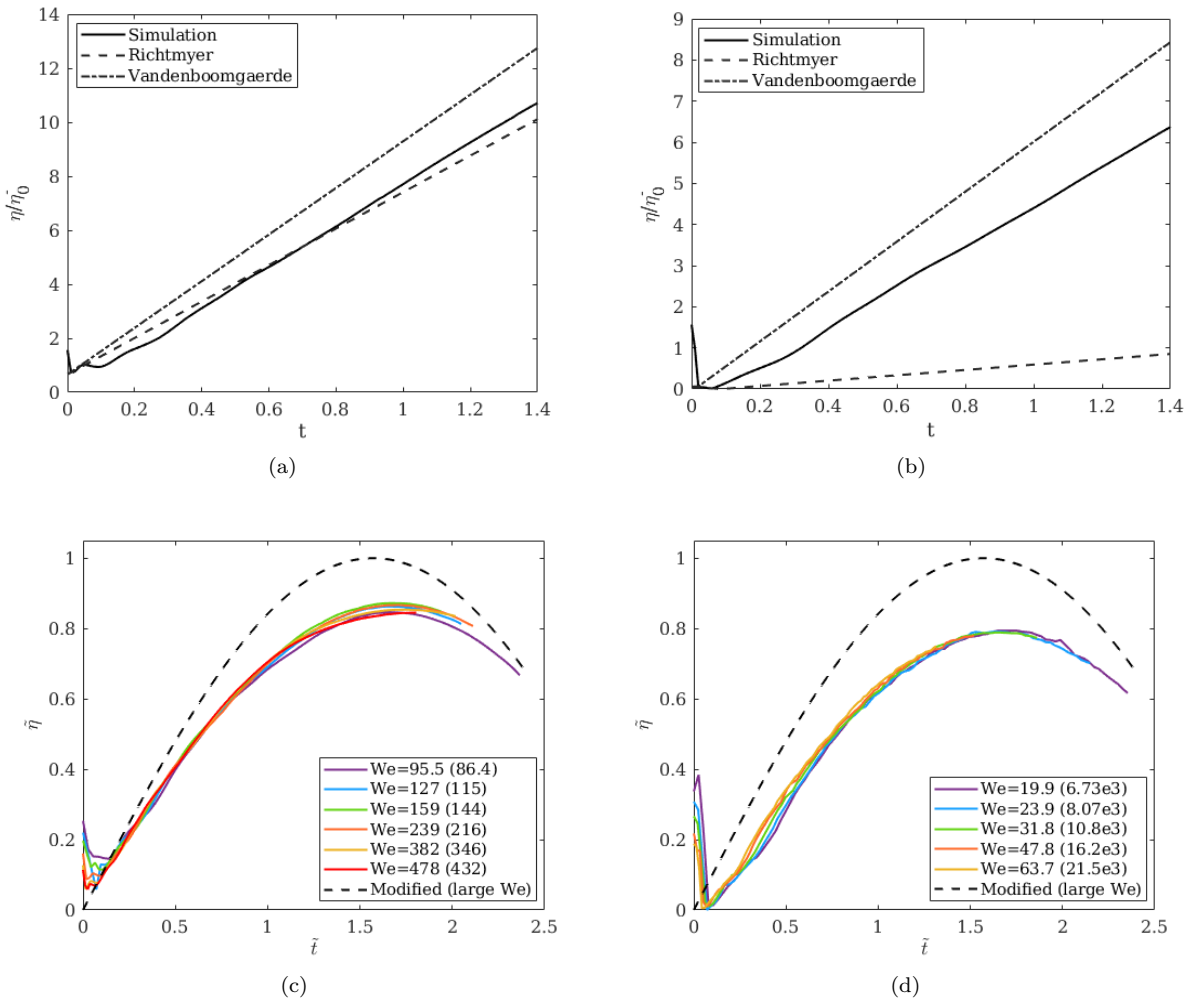

FIG. 4: Upper row: Comparison between the matching of Richtmyer (1960)'s [15] and Vandenboomgaerde et al. (1998) [14]'s theory with simulation data in cases without surface tension; lower row: simulation results scaled using the modified model in cases with surface tension. (a, c): $A^- = 9/11$, (b, d): $A^- = -9/11$. Vandenboomgaerde (1998)'s theory [14] shows a better match with simulation results in both negative and Atwood number cases without surface tension, leading to improved performance of the modified theoretical model.

2. *Effect of incident shock strength*

Apart from surface tension and initial density setups, Mach number of the incident shock $M_{s,i}$ also plays a significant role in the post-shock perturbation growth, as it is directly connected with shock strength and conpressibility's effects. Since Mikaelian's model [5] is essentially impulsive and incorporates Richtmyer's prescription [15], it is natural to expect better matching of the simulation results with our scaled model in the weak shock limit.

However, as is shown in Figure 3(f), the reduce of $M_{s,i}$ from 2 to 1.2 leads to very poor collapsing based on our non-dimensional model. Even though the normalized peaks are generally closer to $\tilde{\eta} = 1$ compared with the strong-shock cases, only the curve of the $We^- = 159.15$ case resembles the prediction by scaled model (7). An unexpected transition zone is detected for Weber numbers between 159.15 and 238.73, where the normalized curves show an abrupt leftward shift accompanied by a drop in peak values. When We^- further increases to 716.2, the normalized curve is noticeably deformed, showing a kink before the first peak.

Figure 3(e) indicates that the cases with We^- beyond 238.73 undergoes potential changes in the flow field near the moving interface. We then seek to verify this by analyzing the development patterns of the interface's moving speed v_I and the local pressure values immediately to the left (p_l) and right (p_r) of the interface. These quantities are normalized by their reference values at $t = 1$ in Figure 5 for the sake of clarity.

The cases with pre-shock Weber number We^- beyond 159.15 experience a simultaneous jump in interface moving velocity and local pressure long after the initial shock-interface interaction period, whose exact location

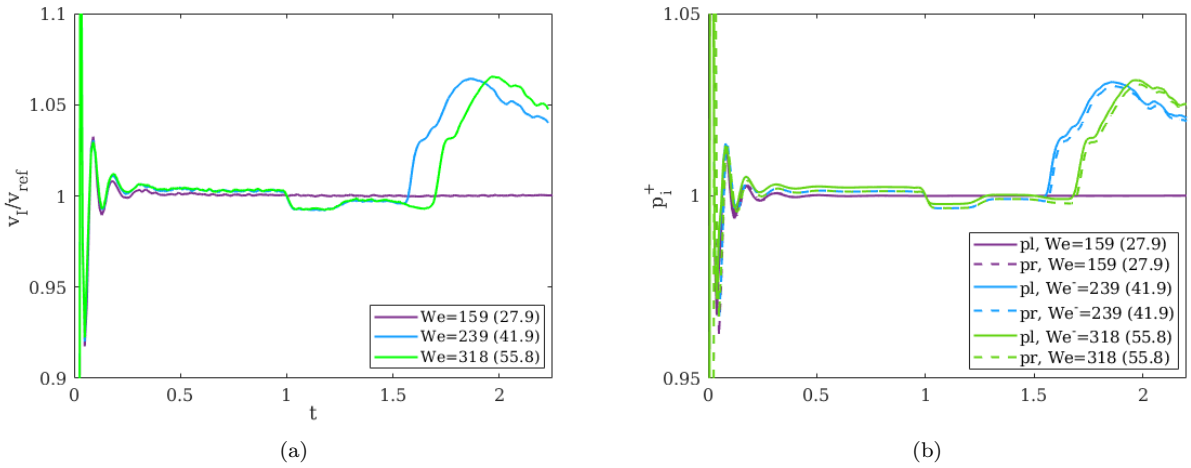

FIG. 5: Tracking of the time development patterns of v_I (a), p_l and p_r (b) for the weak-shock ($M_{s,I} = 1.2$) cases. Jumps in interface velocity and pressure are observed for cases with $We^- = 239$ and 318, which are caused by the interaction of secondary shocks with the interface.

eventually settles at $t = 1.7$ as We^- increases. The jumps are only a few percents in value, after which the interface velocity v_I starts to oscillate and decrease. There is also a slight time delay between the development of p_l and p_r after the jump, which is absent in the case with $We^- = 159$. The subtle kinks in the curves of perturbation amplitude η, e.g. at $t = 3$ in the case with $We^- = 198.94$, occur at the same time with the jumps, indicating a close connection between the two phenomena.

These odd behaviors are identified with continuous late-time interactions between secondary shocks and the moving interface, which are not found in the strong-shock cases. Similar behavior is observed in [27] at $M_{s,I} = 1.2$, where it is found 'an inherently nonlinear and compressible phenomenon' originating from self-interactions at the edges of transmitted and reflected shocks, which is surely out of the incompressible scope of Mikaelian's model [5]. In our case, a secondary shock emanates from the left boundary, which interacts with the interface and causes the jump in local flow fields. Afterwards, perturbed structures develop near the left boundary, from where more pressure waves transmit back to the interface, hence the later high-frequency oscillations.

The absence of similar influences in the $We^- = 159.15$ case and all the strong-shock cases might be caused by stronger curbing effects of surface tension on secondary shocks' interaction with the interface. For the strong-shock cases, the post-shock fluid travels at a higher speed, which might reduce the amount of secondary shocks able to catch up with the moving interface.

Consequently, we conclude that the scaled model (7) based on Mikaelian [5] only stands for the strong-shock positive Atwood number cases, whereas it shows a non-trivial deviation in the peak values of $\tilde{\eta}$, but still keeps good collapsing for the simulation of strong-shock negative Atwood number cases. The negative-Atwood deviation may be reduced by introducing more accurate prescriptions for post-shock initial perturbation growth rate η_0^+. As for the weak-shock cases, the significant reduce in post-shock fluid velocities and surface tension leaves room for the secondary shocks to interact with the interface, which leads to poor collapsing and deviation from the scaled model (7).

C. Nonlinear regime

When surface tension becomes small enough, it can no longer curb the perturbation growth and the late-time development of asymmetric spikes and bubbles on the interface. Figure 6 shows the development of a bubble and spike within the domain for $We^- = 3819.7$. Sizes of the bubble and the spike can be calculated by measuring the difference between the local and average interface positions, whose time derivatives yield bubble velocity U_B and spike velocity U_S.

The measured bubble velocities U_B and spike velocities U_S are plotted against physical time t and shown in Figure 7, where cases with nonlinear and transitional Weber numbers are plotted together. No normalization is applied in Figure 7, as we desire to compare the evolution of bubble velocities of different cases at the same physical time t. Generally speaking, our results agree well in trend with those gained by front-tracking

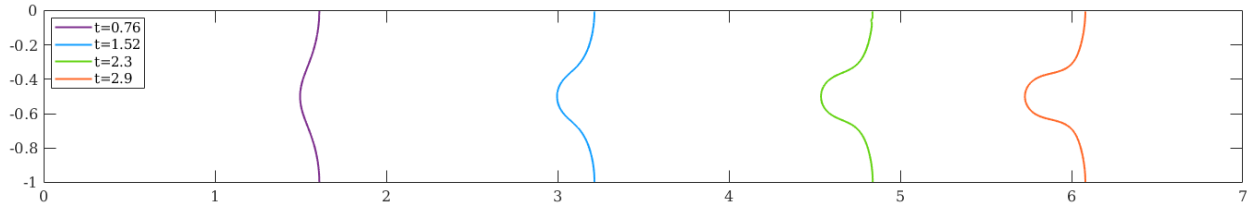

FIG. 6: A series of $We^- = 3819.7$ simulation snapshots showing the perturbed interface's evolution from the initially sinusoidal shape to one with two half-bubbles (across the periodic boundaries) and a spike (at the center) at late time.

techniques in [27].

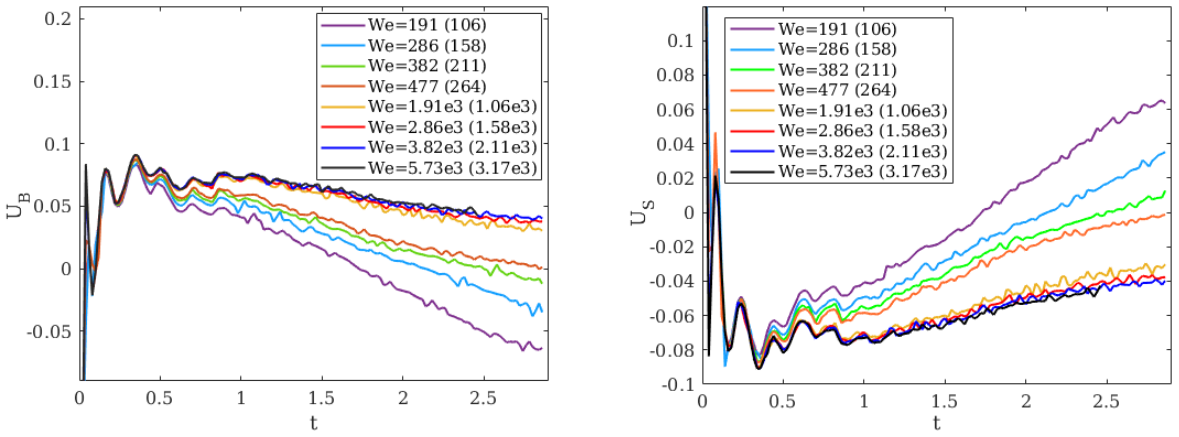

(a) (b)

FIG. 7: Bubble (a) and spike (b) velocity's time development patterns for transitional and nonlinear cases with $A^- = 9/11$. As Weber number increases, the curbing effect of surface tension on the post-shock perturbation growth fades away, and the time development patterns of bubble and spike velocities remain roughly the same within a large range of high Weber numbers (greater than 10^3).

The evolution patterns of bubble velocity are almost the same initially for different Weber numbers, displaying damped oscillating behaviors up to around $t = 0.9$, followed by a constantly decreasing period. Similar early-time oscillations of bubble and spike velocities have been observed in [23], where compressibility is involved; but are lacking in works focusing on incompressible flows (e.g. [11, 28]), indicating that this is an effect of compressibility. Mikaelian [21] reported the oscillations of perturbation growth rate $\dot{\eta}$, and ascribed it to the 'rippling' behavior of the transmitted and reflected shocks; i.e. the two shocks' curvature dies out after they travel a distance of magnitude $\lambda = D$ away from the interface, as is also noted in §II.

Within the decreasing phase of bubble growth rate, for the cases with pre-shock Weber numbers less than 477.46, the 'bubble velocity' (more precisely, the growth rate of the sinusoidal crests as bubbles have not yet formed in these cases) eventually decreases below 0 due to the long-term restoring effect of surface tension. As the Weber number is further increased, the curves remain positive for the entire simulated time and become less sensitive to Weber number beyond $We^- = 1909.8$, with an ultimate bubble velocity U_{Bf} around 0.04 at the end of simulation. This indicates that within this range, the development of bubbles and spikes departs from an oscillatory regime and approaches asymptotically zero velocity. The absolute values of spike velocities $|U_S|$ in the high Weber number cases are also decreasing after the oscillation period, with a final value $|U_{Sf}|$ around 0.04, similar to that of the bubble velocity.

Based on potential flow methods, Sohn derived a nonlinear and incompressible model in [11] for the late-time bubble development, which accounts for both viscosity and surface tension's effects in RMI at the same time. A similar model is also proposed in [29]. Specifically, when the two fluids are inviscid, the non-dimensional expression of Sohn's model [11] reads:

$$\hat{U}_B = \cot \hat{t}, \tag{17}$$

where

$$\hat{U}_B \equiv \frac{3}{A^+}\sqrt{\frac{(1+A^+)\,We^+}{2}}\frac{U_B}{\Delta v}, \quad \hat{t} \equiv \frac{\sqrt{2\,(1+A^+)}}{3+A^+}\tilde{t} = \frac{\sqrt{2\,(1+A^+)}}{3+A^+}\frac{kA^+\Delta v}{\sqrt{We^+}}t \tag{18}$$

We now seek to compare our measured bubble velocities with Sohn's model [11]. For this purpose, we normalize bubble velocity and time extracted from simulation cases with $We^- = 477.46$, 1909.8, 3819.7 and 5729.6 according to the definitions of $\hat{U}_B$ and $\hat{t}$. The normalized curves are plotted in Figure 8 and compared with Sohn's model [11] in the form of (17).

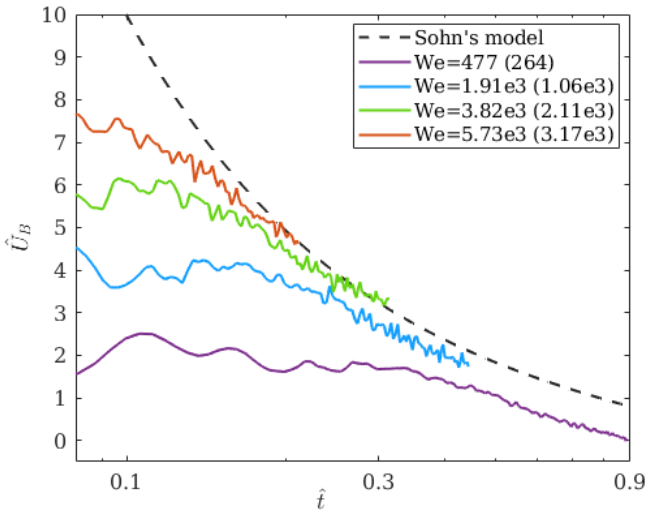

FIG. 8: Comparison between simulated (solid lines) and theoretical (dashed line) bubble velocity developments in cases with $We^- = 477.46$, 1909.8, 3819.7 and 5729.6. Good agreements with Sohn's theory are found at late time and large Weber numbers.

As is shown in the sketch, for the transitional Weber number case with $We^- = 477.46$, Sohn's model [11] significantly overestimates the U_B development within the simulated time range despite correctly capturing the late-time receding trend. As for the cases with higher Weber numbers, where surface tension is weak enough to give way to formation of bubbles and spikes, the normalized simulation results asymptotically converges to Sohn's cotangent model [11] as normalized time $\hat{t}$ increases. Also, as the Weber number increases, convergence to Sohn's model [11] will occur at earlier normalized time $\hat{t}$. This verifies that Sohn's model [11] applies for asymptotically high Weber numbers, since, for lower Weber numbers, surface tension still has some curbing effects on the development of bubbles and spikes.

Within Sohn's text [11], (17) is defined for asymptotically large We^+ so that the singularity at $\hat{t} = \frac{\pi}{2}$ is not reached for any physical time t. However, our simulations feature large but finite We^+, so that for sufficiently large physical time t, the $\hat{t} = \frac{\pi}{2}$ singularity may be reached in simulations. This may correspond with the bubble velocity becoming negative and the interface thus exhibiting nascent oscillatory behavior, as speculated by Sohn [11].

Therefore, we conclude that within the time range investigated, our results agree well with Sohn's model [11] in the bubble-development period of very high Weber number cases, besides the inability of Sohn's model to capture the early oscillatory behaviour of the bubble and spike velocities, due to compressible effects, observed in this study. The development of spikes and bubbles at later time is still to be investigated, especially the eventual breaking-off of spikes from the interface, as has been predicted by Sohn [11] and Matsuoka [30], and recently observed in simulations by Corot et al. [25].

D. Transition to the nonlinear regime

In §IV B, we discussed the linear regime of interface evolution, which occurs for small Weber numbers (strong surface tension), for which the interface perturbations oscillate with small amplitude. Then, in §IV C, we discussed the late-time development of the highly nonlinear bubbles and spikes, which appear for large

Weber numbers (small surface tension). However, for intermediate Weber numbers the surface tension may curb but not prevent transition into a nonlinear evolution regime, which still exhibits oscillatory behavior. The pre-shock initial perturbation amplitude η_0^- also plays a significant role in the later transition process, as larger η_0^- values result in more rapid depositions of baroclinic vorticity at the interface, which causes it to evolve from the initially sinusoidal shape into the complex late-time structures [31]. Therefore, both slope and Weber number will determine the nonlinear transition.

Firstly, we seek a quantitative indicator of nonlinear transition. The earliest such signature is the departure from the sinusoidal oscillation predicted by the linear theory. Therefore, as Weber number and slope increase, nonlinear deviations in the shape of the $\tilde{\eta} - \tilde{t}$ curves are expected to be found first near the normalized peaks, as the onset of nonlinearity should be relatively subtle and achieved most easily at maximum amplitudes. Figures 9a,b,c show the peak of the first perturbation oscillation as a function of Weber number, each at a different η_0^-. In these figures, the axes are normalized according to the linear theory [5]. For $\eta_0^- = 0.02$, lower Weber numbers corresponding with clearly linear oscillations are difficult to attain due to instability of the numerical solver for these parameters.

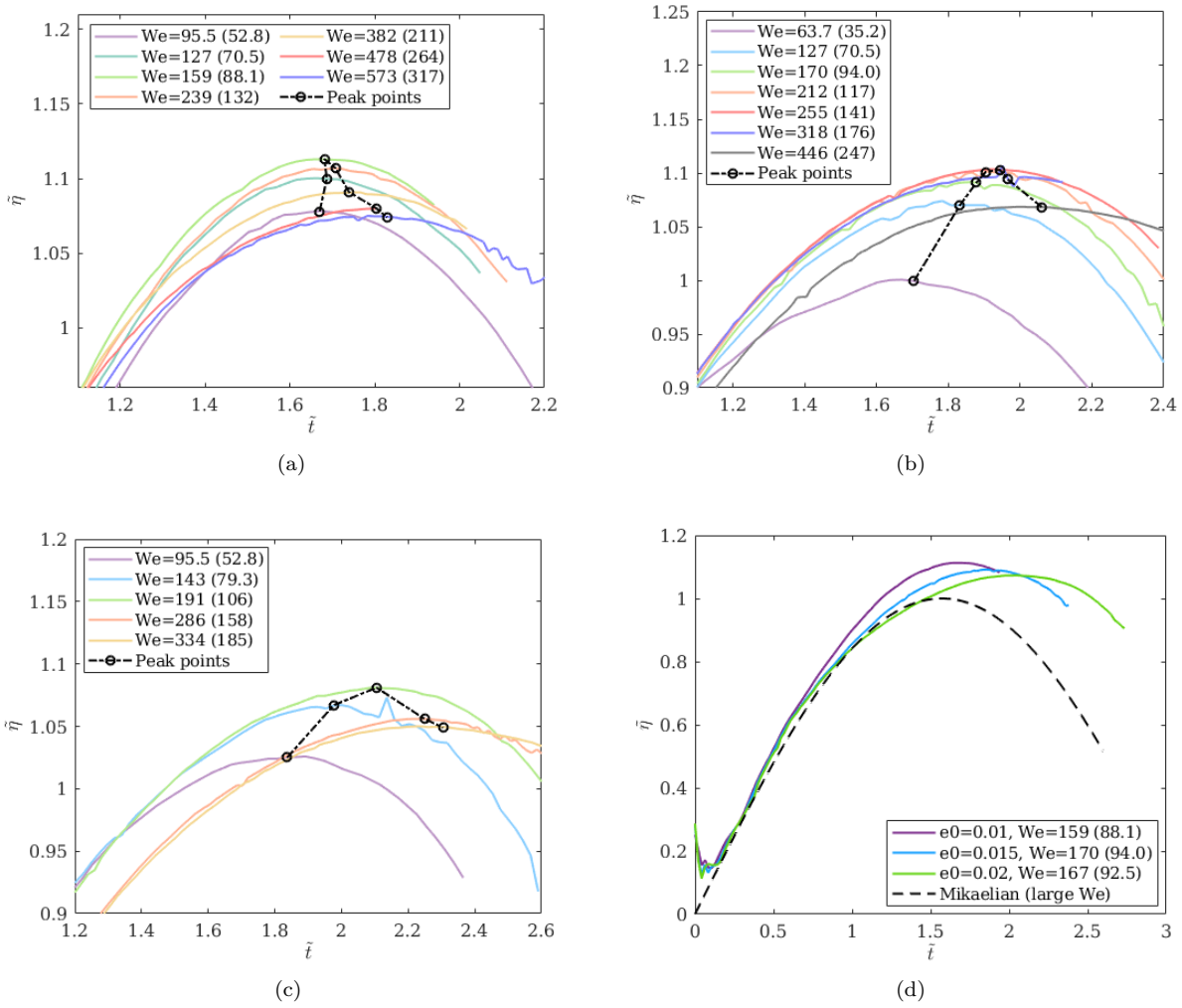

FIG. 9: Nonlinearity detection test results for $A^- = 9/11$. (a): $\eta_0^- = 0.01$; (b): $\eta_0^- = 0.015$; (c): $\eta_0^- = 0.02$; (d): comparisons of cases with $\eta_0^- = 0.01$, 0.015 and 0.02, at We^+ values around 90

For each η_0^-, corresponding with each of Figure 9a,b,c, the peaks of the perturbation amplitude curves are joined according to ascending pre-shock Weber number We^-. In each case, the peak perturbation amplitude first increases, then decreases with increase We^-. The time of peak amplitude, however, increases with We^- in all cases. We also note that this phenomenon becomes apparent at lower Weber numbers for the cases $\eta_0^- = 0.015, 0.02$ (Figure 9b,c) than at $\eta_0^- = 0.01$ (9a). The phase shift that occurs with increasing We^- cannot be explained by the change of $\Delta\varphi = \arctan 1/\sqrt{We^+}$ alone in (7); for example, the phase shift value

predicted by this term for the $\eta_0^- = 0.01$ cases with We^+ between 132.13 and 264.26 is only 0.025, much less than the measured value from Figure 9(a), which should be at least 0.097 as the normalized curve with $We^+ = 264.26$ is still reaching its first peak.

We also varied η_0^- at constant $We^+ \simeq 90$ to see the effect of amplitude alone (Figure 9(d)). Compared with the nonlinear effects of increasing Weber number, the rightward phase shift caused by increasing η_0^- occurs at a global scale, as the normalized curves start to diverge at $\tilde{t} \approx 0.65$, while the peak values decrease slightly as η_0^- increases. Again, this rightward shift cannot be explained by the change of $\Delta\varphi = \arctan 1/\sqrt{We^+}$ in (7), as the term does not explicitly contain η_0^-, and are almost the same for the three cases as the post-shock Weber numbers We^+ are nearly fixed. The initial amplitude of perturbation therefore has a material effect on the critical Weber number required for nonlinear transition.

Therefore, nonlinear transition appears to manifest most clearly as a shift in (normalized) time of the peak of the first oscillation. We quantify this directly as the relative error between the detected peak time (normalized, denoted $\tilde{t}_m$), and that predicted by the linear theory,

$$\Delta \equiv \left| \frac{\tilde{t}_m}{\frac{\pi}{2} - \arctan \frac{1}{\sqrt{We^+}}} - 1 \right|. \tag{19}$$

Note that this is defined according to the post-shock Weber number, We^+. For properly linear evolution, $\Delta = 0$, corresponding to exact matching with the linear theory of [5], but this is not attained for any cases in this study for even the smallest We^-, η_0^-, as discussed in §IV B. Of course, the transition to nonlinearity is also gradual, so that a critical value Δ_c for nonlinear transition can only be heuristically chosen. Here we choose $\Delta_c = 0.25$, and plot in Figure 10a a phase diagram that identifies linear cases ($\Delta < \Delta_c$, in yellow squares) and transitional cases ($\Delta \geq \Delta_c$, in red pluses).

We now seek a simple predictive model for Δ and Δ_c, in order identify the presence of nonlinear effects due to the effect of Weber number We^+ and post-shock perturbation amplitude η_0^+, which appears nondimensionally in the post-shock slope s^+. We assume heuristically that nonlinear effects become apparent when the peak perturbation amplitude-to-wavelength ratio reaches ~ 0.1, or equivalently when $s_{max} \equiv k\eta_{max} \sim 0.6$. From (5),(6) and for $We^+ \gg 1$, this suggests that transition begins to occur for values of the parameter $\chi \simeq 0.6$ where

$$\chi \equiv (s^+)^\alpha \sqrt{We^+} \tag{20}$$

and $\alpha = 1$ as a first estimate.

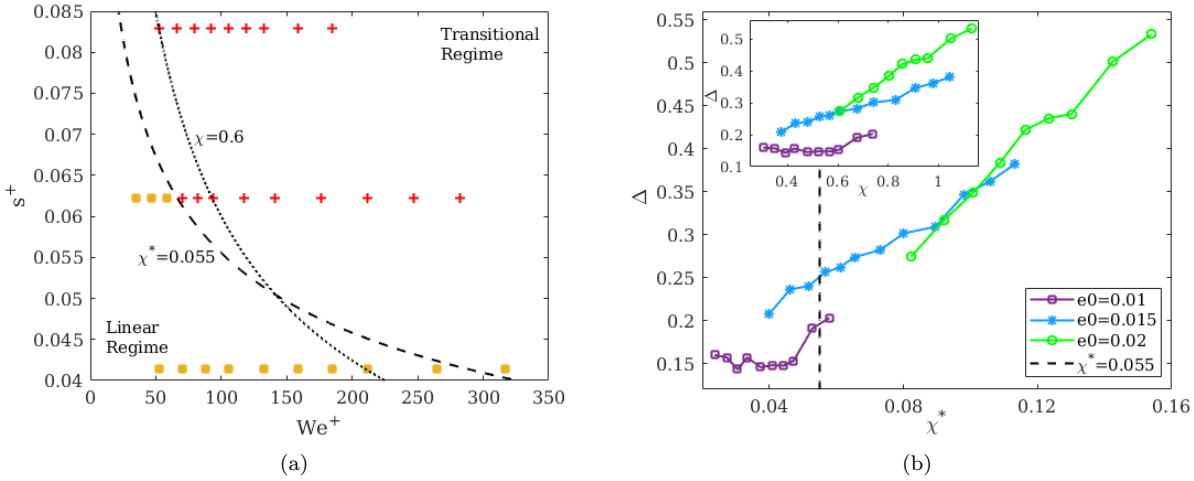

(a) (b)

FIG. 10: (a): Phase diagram showing simulation cases in linear growth-rate regime (purple) and transitional regime (blue). The boundary between the two is selected as $\chi^* = 0.055$ (dashed line), while $\chi = 0.6$ is also plotted in dotted line for comparison; (b): Relationship between Δ and χ with different s^- setups. A common growth stage of Δ is reached for different s^- setups as χ^* increases.

We plot $\chi = 0.6$ in Figure 10(a) as a dotted line, but it does not correctly delineate linear and transitional cases. Moreover, as shown in the inset of Figure 10(b), χ does not fully explain the variation in Δ. In that plot, while Δ increases with χ, the rate of increase is clearly dependent on η_0^- (hence s^- and therefore s^+).

There is therefore a further dependence of the transition to nonlinearity on s^+, suggesting a better choice of α in (20), which might be related to the local competition of surface tension and baroclinic vorticity on the interface, and awaits a more detailed investigation. Figure 10(b) shows the resulting scaling with a modified χ^* where $\alpha = 1.8$, which better collapses the data as the consistent growth trend of the $\eta_0^- = 0.02$ cases now aligns well with the last several cases of both $\eta_0^- = 0.01$ and 0.015. Plotting the dashed line $\chi^* = 0.055$ on Figure 10(a) also more clearly delineates the linear and nonlinear cases. Based on this, we conclude that $\chi^* = 0.055$ is the useful criterion for determining transition out of the linear to the nonlinear regime.

V. CONCLUSIONS

We have presented nonlinear, compressible numerical simulations of the Richtmyer-Meshkov instability with surface tension. Using appropriate dimensional analysis, we find that the existing theoretical impulsive model due to [5] predicts well the interfacial evolution of the shocked interface, with an appropriate modification to accommodate Atwood number of either sign. At low incident Mach number, the numerical results differ from the impulsive model due directly to boundary effects in our problem formulation, but thereby indicate some sensitivity of the impulsive model to compressible effects at low Mach number and weak surface tension. Next, within the nonlinear regime, we also show agreement with theoretical results in the asymptotic (large time) bubble velocity in the limit of weak surface tension. Finally, we find an heuristic criterion for transition to nonlinear evolution (that is, nonlinear deviation from the impulsive model) based on initial perturbation slope and Weber number.

These results indicate the utility of this numerical model for problems of this kind, and constitute a further validation of its surface tension model and implementation. This study is also a stepping stone towards the mixed compressible-incompressible problem which may influence the early-time development of the shocked-droplet or aerobreakup problem [32].

Appendix A: Numerical convergence

Since each fluid is inviscid, the smallest length scale in the bulk is set by numerical dissipation, so that pointwise grid convergence is not expected. Nevertheless, we require that the primary characteristics of the RMI growth, both with and without surface tension, be independent of grid resolution at our chosen resolution of $L = 9$. Here, four groups of convergence tests are conducted in total for four different categories of initial setups; namely, light-heavy ($A^- > 0$) and heavy-light ($A^- < 0$) density setups with and without surface tension. Specifically, we set $A^- = \pm 9/11$, while $We^- = +\infty$ or 159.15.

The raw outputs of the tests are provided in Figure 11, where the absolute values of post-shock amplitude ratio $|\eta/\eta_0^-|$ is plotted against physical time t. Absolute values are taken to facilitate the comparison between the results of light-heavy and heavy-light initial density setups, as in the latter case there will be a phase reversal of the perturbation profile. The noise-signal ratio in the simulation output files is especially large up to the end of the early-time shock-interface interaction period, which causes inaccuracies in the extracted values of η; also, when relatively weak surface tension is introduced to the heavy-light density setup case, noise is found in the neighborhood of the interface throughout the simulation, causing spurious high-frequency oscillations on the entire curve. Despite these problems, we still observe good converging trend at resolution level $L = 9$ for all four groups of convergence tests.

In order to better quantify the convergence behavior, we select the numerical integral of $|\eta/\eta_0^-|$ over the time range of [0.05, 1.4] as the convergence metric, following [22]. When $We^- = 159.15$, this metric shows a monotonous convergence for the $A^- = -9/11$ cases with an estimated relative error of 2.2% at Level 9, and an oscillatory convergence for the $A^- = 9/11$ ones with an uncertainty of 2.0% [33].

Appendix B: Determination of post-shock state

While in this study, the post-shock state is determined through numerical diagnostics, it is instructive to compare them with theoretical predictions.

Mikaelian [21] proposes a set of equations for determination of the post-shock parameters for the RMI *without* surface tension. Lying at the core of this system are two alternative transcendental equations (Equations A4

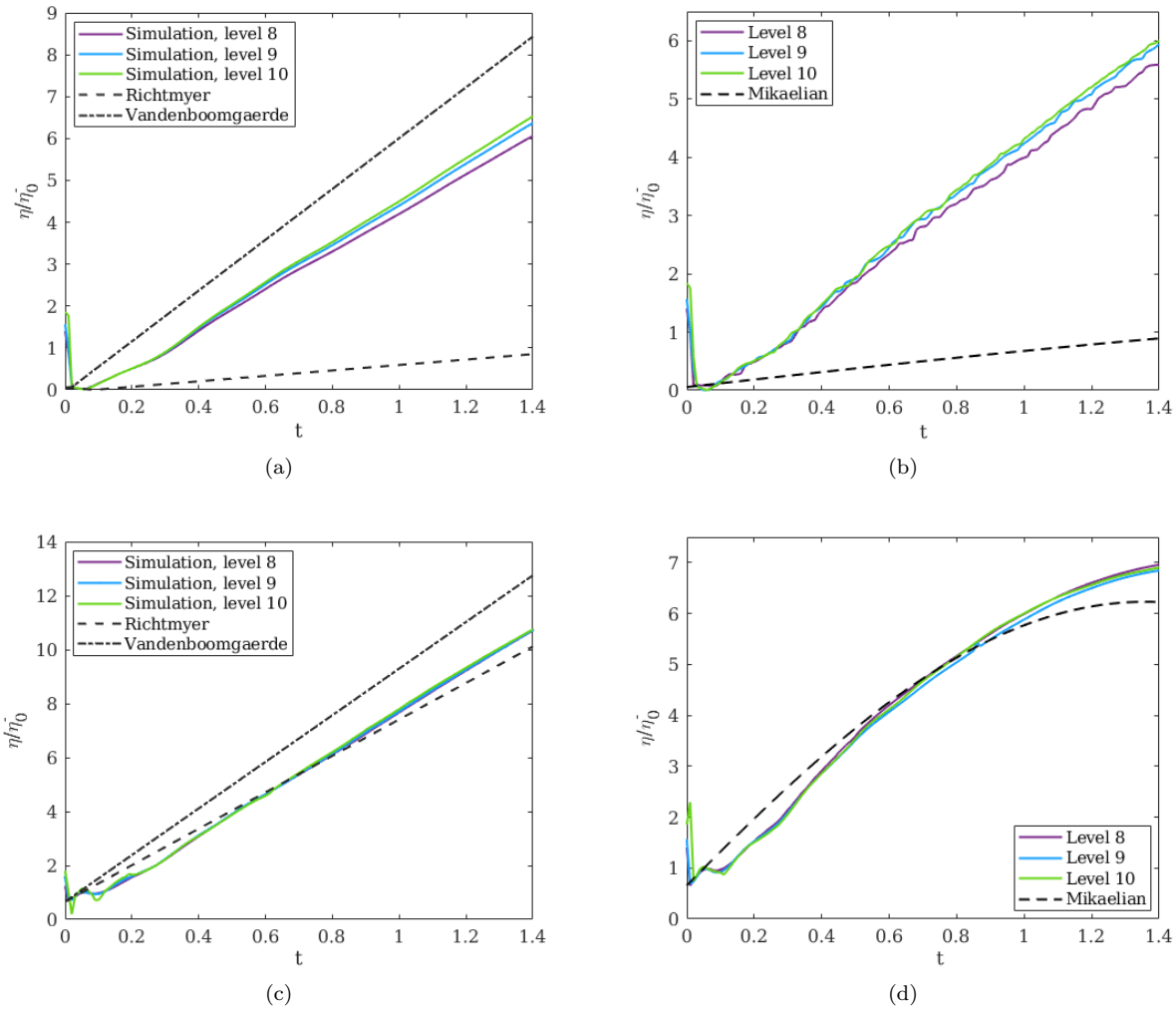

FIG. 11: Convergence test results (Upper row: heavy-light density setup without (a) and with (b) surface tension; lower row: light-heavy density setup without (c) and with (d) surface tension). Good numerical convergence is observed for all the inviscid test cases.

and A16 in the appendix of [21]) for which there are generally no analytical solutions:

$$\frac{\xi - \frac{p_0}{p_L}}{\sqrt{\xi + \frac{\gamma-1}{\gamma+1}\frac{p_0}{p_L}}} = \begin{cases} \sqrt{\frac{\rho_2^-}{\rho_1^-}} \cdot \frac{1 - \frac{p_0}{p_L} - (\xi - 1)\sqrt{\frac{\gamma - 1 + (\gamma+1)\frac{p_0}{p_L}}{(\gamma+1)\xi + \gamma - 1}}}{\sqrt{1 + \frac{\gamma-1}{\gamma+1}\frac{p_0}{p_L}}}, & \xi \geq 1 \\ \sqrt{\frac{\rho_2^-}{\rho_1^-}} \cdot \frac{1 - \frac{p_0}{p_L} + \left(1 - \xi^{\frac{\gamma-1}{2\gamma}}\right)\sqrt{\frac{2\gamma}{\gamma-1} + \frac{\gamma+1}{(\gamma-1)^2}\frac{p_0}{p_L}}}{\sqrt{1 + \frac{\gamma-1}{\gamma+1}\frac{p_0}{p_L}}}, & \xi < 1 \end{cases} \tag{B1}$$

The first equation is physically valid when its root satisfies $\xi \geq 1$, which indicates a reflected shock; otherwise, the second one will produce a root satisfying $\xi \leq 1$, which indicates a reflected rarefaction instead. Once the

value of ξ has been determined, the post-shock quantities $\rho_i^+, \Delta v$ can be determined via the following equations,

$$\begin{aligned}
\frac{\rho_1^+}{\rho_1^-} &= \begin{cases} \dfrac{(\gamma+1)+(\gamma-1)\frac{p_0}{p_L}}{(\gamma-1)+(\gamma+1)\frac{p_0}{p_L}} \cdot \dfrac{(\gamma+1)\xi+\gamma-1}{(\gamma-1)\xi+\gamma+1}, \ \xi \geq 1 \\ \dfrac{(\gamma+1)+(\gamma-1)\frac{p_0}{p_L}}{(\gamma-1)+(\gamma+1)\frac{p_0}{p_L}} \cdot \xi^{\frac{1}{\gamma}}, \ \xi < 1 \end{cases} \\
\frac{\rho_2^+}{\rho_2^-} &= \frac{(\gamma+1)\xi+(\gamma-1)\frac{p_0}{p_L}}{(\gamma-1)\xi+(\gamma+1)\frac{p_0}{p_L}} \\
(\Delta v)^2 &= \frac{2\xi p_L}{\rho_2^-} \cdot \frac{\left(1-\frac{p_0}{\xi p_L}\right)^2}{(\gamma+1)+(\gamma-1)\frac{p_0}{\xi p_L}}
\end{aligned} \tag{B2}$$

It should be noted that equation sets (B1, B2) do not include effects of surface tension or the perturbed interface profile investigated in our work. In particular, due to the perturbed interface profile, the transmitted and reflected wavefronts both have corrugated shapes initially, which are similar to the sinusoidal shape of the perturbed interface itself. These wavefront corrugations will oscillate and die out after the waves travel a distance of several wavelengths away from the post-shock interface [34], as is the situation shown in Figure 1(b). This rippling behavior has been observed in the experiments of [35], and reproduced afterwards in many simulation works (e.g. [21, 27, 36]).

We compare now the predictions of theory and numerical diagnostics for the cases presented in Figure 2. The transcendental equation sets ((B1), (B2)) yields $\xi = 1.8982$ for the cases with $A^- = 9/11$, and $\xi = 0.4668$ for those with $A^- = -9/11$. These solutions agree with the categorization of reflected wave (Equation 8) by Drake [18], which is based on the sign of pre-shock Atwood number A^-.

The post-shock parameters are then derived using the solution ξ, and their comparisons with the values of numerical diagnostics measured at around $t = 0.4$ are shown in the following Table I:

A^- (Method)	9/11 (ND)	9/11 (ES)	−9/11 (ND)	−9/11 (ES)
ρ_1^+	0.356	0.418	1.700	1.548
ρ_2^+	3.084	3.593	0.169	0.168
A^+	0.793	0.792	-0.819	-0.804
Δv	2.030	2.333	2.231	2.109
r	0.66	0.688	0.0565	0.109

TABLE I: Comparison between post-shock values gained from numerical diagnostics ("ND") and equation solving ("ES").

Within each pre-shock Atwood number category, the results gained via numerical diagnostics and equation solving for the same post-shock parameter are roughly on the same level of magnitude. Particularly good agreements are found for ρ_2^+ values in cases with $A^- = -9/11$, and also A^+ and r in those with $A^- = 9/11$. However, generally speaking, nontrivial discrepancies do exist between the results of the two solving methods.

The discrepancies are most likely caused by the equation system (B1) 's not accounting for the influence of the post-shock wavefronts' 'rippling' behavior (see §II). In cases without surface tension, such behavior is reported in [21] to cause the post-shock perturbation growth rate $\dot{\eta}$ to reach an asymptotic value, for which no simple analytic solution exists [21, 37], after going through a damped oscillation period, which also matches the trend of our results in Figure 2.

The ascription of discrepancies above is further consolidated by the following observation. As is shown in Figure 2, for the case with $A^- = 9/11$, our state diagnostic case captures $\rho_1^+ = 0.411$ and $\rho_2^+ = 3.590$ at a very early time $t = 0.02$ after the shock-interface interaction, which matches very well with the solution of [21]'s equation sets (see column 3 of Table I). However, the two densities eventually settle down at the steady-state

values, as discussed in §IV A.

[1] John Lindl, Otto Landen, John Edwards, Ed Moses, and NIC team. Review of the national ignition campaign 2009-2012. *Physics of Plasmas*, 21(2):020501, 2014.

[2] Nicholas Gibbons, Rolf Gehre, Stefan Brieschenk, and Vincent Wheatley. Blast wave-induced mixing in a laser ignited hypersonic flow. *Journal of Fluids Engineering*, 140(5), 2018.

[3] David Arnett. The role of mixing in astrophysics. *The Astrophysical Journal Supplement Series*, 127(2):213, 2000.

[4] Takayoshi Sano, Katsunobu Nishihara, Chihiro Matsuoka, and Tsuyoshi Inoue. Magnetic field amplification associated with the richtmyer-meshkov instability. *The Astrophysical Journal*, 758(2):126, 2012.

[5] Karnig O Mikaelian. Rayleigh-taylor and richtmyer-meshkov instabilities in multilayer fluids with surface tension. *Physical Review A*, 42(12):7211, 1990.

[6] Pierre Carlès and Stéphane Popinet. The effect of viscosity, surface tension and non-linearity on richtmyer–meshkov instability. *European Journal of Mechanics-B/Fluids*, 21(5):511–526, 2002.

[7] TG Theofanous. Aerobreakup of newtonian and viscoelastic liquids. *Annual Review of Fluid Mechanics*, 43:661–690, 2011.

[8] Jomela C Meng and Tim Colonius. Numerical simulation of the aerobreakup of a water droplet. *Journal of Fluid Mechanics*, 835:1108, 2018.

[9] Martin Brouillette. The richtmyer-meshkov instability. *Annual Review of Fluid Mechanics*, 34(1):445–468, 2002.

[10] SI Abarzhi and M Herrmann. New type of the interface evolution in the richtmyer-meshkov instability. Technical report, CENTER FOR TURBULENCE RESEARCH STANFORD CA, 2003.

[11] Sung-Ik Sohn. Effects of surface tension and viscosity on the growth rates of rayleigh-taylor and richtmyer-meshkov instabilities. *Physical Review E*, 80(5):055302, 2009.

[12] Hang Ding, Peter DM Spelt, and Chang Shu. Diffuse interface model for incompressible two-phase flows with large density ratios. *Journal of Computational Physics*, 226(2):2078–2095, 2007.

[13] Daniel Fuster and Stéphane Popinet. An all-mach method for the simulation of bubble dynamics problems in the presence of surface tension. *Journal of Computational Physics*, 374:752–768, 2018.

[14] Marc Vandenboomgaerde, Claude Mügler, and Serge Gauthier. Impulsive model for the richtmyer-meshkov instability. *Physical Review E*, 58(2):1874, 1998.

[15] Robert D. Richtmyer. Taylor instability in shock acceleration of compressible fluids. *Communications on Pure and Applied Mathematics*, 13(2):297–319, 1960.

[16] Alexander L Velikovich. Analytic theory of richtmyer–meshkov instability for the case of reflected rarefaction wave. *Physics of Fluids*, 8(6):1666–1679, 1996.

[17] AL Velikovich, Marcus Herrmann, and SI Abarzhi. Perturbation theory and numerical modelling of weakly and moderately nonlinear dynamics of the incompressible richtmyer-meshkov instability. *Journal of fluid mechanics*, 751:432, 2014.

[18] R. Paul Drake. *Shocks and Rarefactions*, pages 107–167. Springer Berlin Heidelberg, Berlin, Heidelberg, 2006.

[19] KA Meyer and PJ Blewett. Numerical investigation of the stability of a shock-accelerated interface between two fluids. *The Physics of Fluids*, 15(5):753–759, 1972.

[20] Yumin Yang, Qiang Zhang, and David H Sharp. Small amplitude theory of richtmyer–meshkov instability. *Physics of Fluids*, 6(5):1856–1873, 1994.

[21] Karnig O Mikaelian. Freeze-out and the effect of compressibility in the richtmyer-meshkov instability. *Physics of Fluids*, 6(1):356–368, 1994.

[22] W Mostert, V Wheatley, Ravi Samtaney, and DI Pullin. Effects of magnetic fields on magnetohydrodynamic cylindrical and spherical richtmyer-meshkov instability. *Physics of Fluids*, 27(10):104102, 2015.

[23] Richard L Holmes, Guy Dimonte, Bruce Fryxell, Michael L Gittings, John W Grove, Marilyn Schneider, David H Sharp, Alexander L Velikovich, Robert P Weaver, and Qiang Zhang. Richtmyer–meshkov instability growth: experiment, simulation and theory. *Journal of Fluid Mechanics*, 389:55–79, 1999.

[24] Alexei D Kotelnikov, Jaideep Ray, and Norman J Zabusky. Vortex morphologies on reaccelerated interfaces: Visualization, quantification and modeling of one-and two-mode compressible and incompressible environments. *Physics of fluids*, 12(12):3245–3264, 2000.

[25] T Corot, P Hoch, and Emmanuel Labourasse. Surface tension for compressible fluids in ale framework. *Journal of Computational Physics*, 407:109247, 2020.

[26] Juan Gustavo Wouchuk and Katsunobu Nishihara. Asymptotic growth in the linear richtmyer–meshkov instability. *Physics of Plasmas*, 4(4):1028–1038, 1997.

[27] Richard L. Holmes, John W. Grove, and David H. Sharp. Numerical investigation of richtmyer–meshkov instability using front tracking. *Journal of Fluid Mechanics*, 301:51–64, 1995.

[28] Chihiro Matsuoka. Vortex sheet motion in incompressible richtmyer–meshkov and rayleigh–taylor instabilities with surface tension. *Physics of Fluids*, 21(9):092107, 2009.

[29] MR Gupta, Rahul Banerjee, LK Mandal, R Bhar, HC Pant, Manoranjan Khan, and MK Srivastava. Effect of viscosity and surface tension on the growth of rayleigh–taylor instability and richtmyer–meshkov instability induced two fluid interfacial nonlinear structure. *Indian Journal of Physics*, 86(6):471–479, 2012.

[30] Chihiro Matsuoka. Nonlinear behavior of a vortex sheet in incompressible richtmyer–meshkov instability with surface tension. *Physica Scripta*, 2008(T132):014042, 2008.
[31] Chihiro Matsuoka, Katsunobu Nishihara, and Yuko Fukuda. Nonlinear evolution of an interface in the richtmyer-meshkov instability. *Physical Review E*, 67(3):036301, 2003.
[32] TG Theofanous, VV Mitkin, and CL Ng. The physics of aerobreakup. iii. viscoelastic liquids. *Physics of Fluids*, 25(3):032101, 2013.
[33] Fred Stern, Robert V Wilson, Hugh W Coleman, and Eric G Paterson. Comprehensive approach to verification and validation of cfd simulations—part 1: methodology and procedures. *J. Fluids Eng.*, 123(4):793–802, 2001.
[34] K Nishihara, JG Wouchuk, C Matsuoka, R Ishizaki, and VV Zhakhovsky. Richtmyer–meshkov instability: theory of linear and nonlinear evolution. *Philosophical Transactions of the Royal Society A: Mathematical, Physical and Engineering Sciences*, 368(1916):1769–1807, 2010.
[35] EE Meshkov. Instability of the interface of two gases accelerated by a shock wave. *Fluid Dynamics*, 4(5):101–104, 1969.
[36] Karnig O Mikaelian. Effect of viscosity on rayleigh-taylor and richtmyer-meshkov instabilities. *Physical Review E*, 47(1):375, 1993.
[37] Gary Fraley. Rayleigh–taylor stability for a normal shock wave–density discontinuity interaction. *The Physics of fluids*, 29(2):376–386, 1986.